Astronomy & Astrophysics

The qWR star HD 45166[*],[**]

II. Fundamental stellar parameters and evidence of a latitude-dependent wind

J. H. Groh[1,2], A. S. Oliveira[3,4], and J. E. Steiner[2]

1 Max-Planck-Institut für Radioastronomie, Auf dem Hügel 69, 53121 Bonn, Germany
   e-mail: jgroh@mpifr-bonn.mpg.de
2 Instituto de Astronomia, Geofísica e Ciências Atmosféricas, Universidade de São Paulo, Rua do Matão 1226, Cidade Universitária,
   05508-900 São Paulo, SP, Brazil
3 IP&D, Universidade do Vale do Paraíba, Av. Shishima Hifumi 2911, CEP 12244-000, São José dos Campos, SP, Brazil
4 SOAR Telescope, Casilla 603, La Serena, Chile

ABSTRACT

Context. The enigmatic object HD 45166 is a qWR star in a binary system with an orbital period of 1.596 day, and presents a rich emission-line spectrum in addition to absorption lines from the companion star (B7 V). As the system inclination is very small ($i = 0.77° \pm 0.09°$), HD 45166 is an ideal laboratory for wind-structure studies.
Aims. The goal of the present paper is to determine the fundamental stellar and wind parameters of the qWR star.
Methods. A radiative transfer model for the wind and photosphere of the qWR star was calculated using the non-LTE code CMFGEN. The wind asymmetry was also analyzed using a recently-developed version of CMFGEN to compute the emerging spectrum in two-dimensional geometry. The temporal-variance spectrum (TVS) was calculated to study the line-profile variations.
Results. Abundances and stellar and wind parameters of the qWR star were obtained. The qWR star has an effective temperature of $T_{\rm eff} = 50\,000 \pm 2000$ K, a luminosity of $\log(L/L_\odot) = 3.75 \pm 0.08$, and a corresponding photospheric radius of $R_{\rm phot} = 1.00\,R_\odot$. The star is helium-rich ($N({\rm H})/N({\rm He}) = 2.0$), while the CNO abundances are anomalous when compared either to solar values, to planetary nebulae, or to WR stars. The mass-loss rate is $\dot{M} = 2.2 \times 10^{-7}\,M_\odot\,{\rm yr}^{-1}$, and the wind terminal velocity is $v_\infty = 425$ km s^{-1}. The comparison between the observed line profiles and models computed under different latitude-dependent wind densities strongly suggests the presence of an oblate wind density enhancement, with a density contrast of at least 8:1 from equator to pole. If a high velocity polar wind is present ($\sim$1200 km s^{-1}), the minimum density contrast is reduced to 4:1.
Conclusions. The wind parameters determined are unusual when compared to O-type stars or to typical WR stars. While for WR stars $v_\infty/v_{\rm esc} > 1.5$, in the case of HD 45166 it is much smaller ($v_\infty/v_{\rm esc} = 0.32$). In addition, the efficiency of momentum transfer is $\eta = 0.74$, which is at least 4 times smaller than in a typical WR. We find evidence for the presence of a wind compression zone, since the equatorial wind density is significantly higher than the polar wind. The TVS supports the presence of such a latitude-dependent wind and a variable absorption/scattering gas near the equator.

Key words. stars: winds, outflows – stars: mass-loss – stars: fundamental parameters – binaries: spectroscopic –
stars: individual: HD 45166 – stars: Wolf-Rayet

1. Introduction

HD 45166 has been observed since 1922 (Anger 1933), without much advancement in the understanding of its nature. van Blerkom (1978) analyzed the optical H and He lines assuming that HD 45166 is a Population I WR object, and concluded that the WR component has a radius of 1 $R_\odot$, and has a small envelope expanding with a velocity of 150 km s^{-1}. The resulting number density of He II is about 10^{11} cm^{-3} and mimics the environment of a WR envelope. He found a mass-loss rate of $4.5 \times 10^{-8}\,M_\odot\,{\rm yr}^{-1}$, and wind densities of $N({\rm He}) = 3 \times 10^{11}$ cm^{-3} and $N({\rm H}) = 10^{12}$ cm^{-3}. Analyzing the IUE data, Willis & Stickland (1983) derived $\log(L/L_\odot) = 3.84$, a radius of $R = 0.77\,R_\odot$, and an effective temperature of $T_{\rm eff} = 60\,000$ K. Willis et al. (1989) obtained a wind terminal velocity of 1200 km s^{-1}, derived from the UV resonance lines. Recently, Willis & Burnley (2006) analyzed the far-ultraviolet spectrum of HD 45166. By fitting the

continuum energy distribution from the far ultraviolet to the near-infrared, they derived that the qWR star has $R = 1.20\,R_\odot$, $\log(L/L_\odot) = 3.28$, and $T_{\rm eff} = 35\,000$ K. A mass-loss rate of $2 \times 10^{-7}\,M_\odot\,{\rm yr}^{-1}$ was inferred by those authors using the optical lines of He II, C III, and N III.

Steiner & Oliveira (2005, hereafter Paper I) showed that HD 45166 is a double-lined binary system composed of a qWR and a B7 V star in a system with an orbital period of 1.596 day. HD 45166 presents a rich emission-line spectrum in addition to the absorption spectrum due to the cooler component. The orbital parameters of the system were derived in Paper I, showing that the orbit is slightly eccentric ($e = 0.18 \pm 0.08$) and has a very small inclination angle ($i = 0.77° \pm 0.09°$). The masses are $M_1 = 4.2\,M_\odot$ and $M_2 = 4.8\,M_\odot$. In addition to the orbital period, two other periods were found in the qWR star (5 and 15 h, Paper I). As the system inclination is very small, HD 45166 is an interesting laboratory to study the wind structure.

The goal of the present paper is to study in detail the stellar and wind parameters of the qWR star. For this purpose we use the radiative transfer code CMFGEN (Hillier & Miller 1998) to analyze the high-resolution optical spectrum presented

---

in Paper I. The temporal variance spectrum (hereafter TVS; Fullerton et al. 1996) of the strongest emission lines is also analyzed in order to obtain insights into the wind structure.

This paper is organized as follows. In Sect. 2, we briefly summarize the data presented in Paper I, and describe how the spectrum of the qWR star was disentangled from the B7 V companion. In Sect. 3, we present the main characteristics of CMFGEN, while in Sect. 4 the results of the quantitative analysis using the spherical modeling are shown. The latitude dependence of the wind is analyzed in Sect. 5, using a recently-developed version of CMFGEN (Busche & Hillier 2005). The analysis of the TVS is presented in Sect. 6, and the results obtained in this work are discussed in Sect. 7, especially the presence of a wind-compression zone. Section 8 summarizes the main conclusions of this paper.

2. Observations and subtraction of the B7 V companion spectrum

The data analyzed in this paper were taken in January 2004 with the Fiber-fed Extended Range Optical Spectrograph (FEROS, Kaufer et al. 1999) at the 1.52 m telescope of the European Southern Observatory (ESO) in La Silla, Chile. The spectra have a resolution power of $R = 48\,000$, and were reduced using the standard data-reduction pipeline (Stahl et al. 1999). A total of 40 spectra with individual exposure times of 15 min were averaged, resulting in a total integration time of 10 h.

Since our goal in this paper is to obtain the fundamental parameters of the qWR star, its spectrum has first to be disentangled from the spectrum of the B7 V companion. This task was accomplished by:

1. flux calibrating the average observed spectrum of HD 45166 using the available photometry (de-reddened);
2. scaling the flux of a standard synthetic B7 V continuum spectrum, obtained from Pickles (1998), to a distance of 1.3 kpc (Paper I);
3. multiplying the normalized spectrum of the B7 V star HD 62714 obtained from the UVES Paranal Observatory Project (Bagnulo et al. 2003) by the Pickles B7 V scaled continuum obtained above, to account for the spectral features of the B7 V companion;
4. subtracting this scaled B7 V spectrum from the flux-calibrated observed spectrum of HD 45166;
5. normalizing the resultant spectrum by the continuum, which can then be directly compared to the continuum-normalized model spectrum.

In general, this procedure results in a very good subtraction of the continuum and reasonable subtraction of the hydrogen absorption lines due to the B7 V star, as can be seen in Fig. 1. However, the rest of the rich absorption-line spectrum of the companion star is not subtracted perfectly, and weak residual lines can still be seen. Nevertheless, their presence do not affect the diagnostic lines used for obtaining the parameters of the qWR, as the companion lines are quite narrow, weak, and often are not blended with the lines of the qWR star.

3. The model

We used the radiative transfer code CMFGEN (Hillier & Miller 1998) to analyze the spectrum of the hot component of HD 45166 in detail. The code assumes a spherically-symmetric
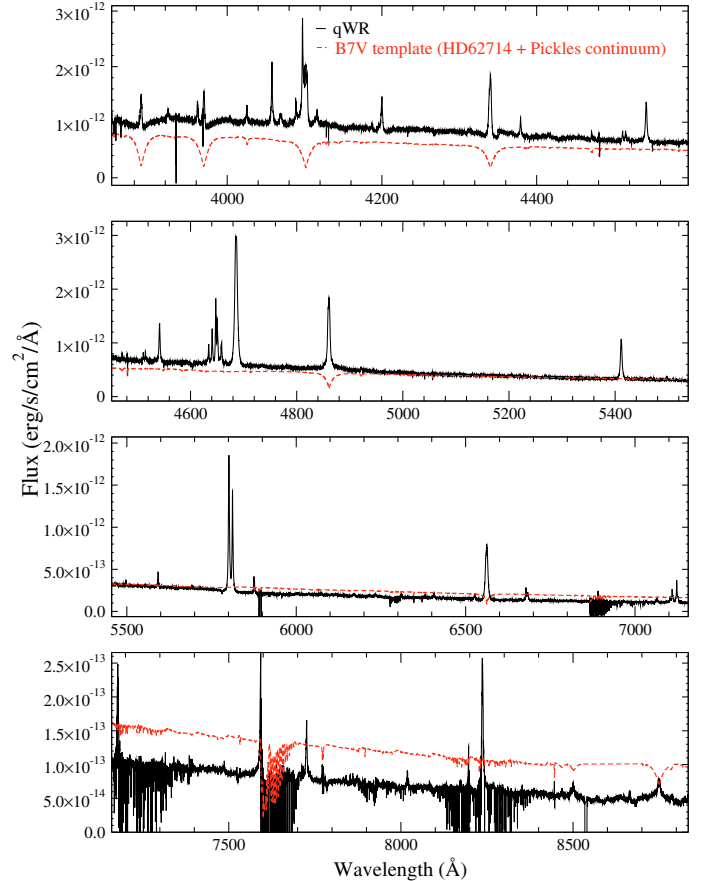
Fig. 1. Resulting de-reddened spectrum of HD 45166 decomposed into the qWR star (full black line) and the B7 V companion (dashed red line). As anticipated in Paper I, the qWR star is dominant in the blue part of the spectrum, while the B7 V companion dominates for $\lambda > 5000$ Å.

outflow in steady-state, computing line and continuum formation in the non-LTE regime. Each model is specified by the hydrostatic core radius $R_\star$, the luminosity $L_\star$, the mass-loss rate $\dot{M}$, the wind terminal velocity v_∞, and the chemical abundances Z_i of the included species. Since the code does not solve the momentum equation of the wind, a velocity law must be adopted. The velocity structure $v(r)$ is parameterized by a beta-type law, which is modified at depth to smoothly match a hydrostatic structure at $R_\star$ (defined at a Rosseland optical depth of $\tau = 100$ in our models). *The use of a hydrostatic structure at depth is crucial to analyze HD 45166, since the continuum and some of the higher ionization lines are formed in this region.*

The code includes the effects of clumping via a volume filling factor f which depends on the distance following an exponential law that supposes an unclumped wind when $r = R_\star$. The clumps start to form at the distance where $v = v_c$, and the wind reaches its maximum clumping at large r:

$$f(r) = f + (1 - f)\exp[-v(r)/v_c]. \tag{1}$$

CMFGEN directly includes the influence of line blanketing in the ionization structure of the wind and, consequently, in the calculated spectrum. With the concept of super-levels, the equations of statistical equilibrium and radiative transfer can be solved simultaneously including thousands of lines in NLTE. The atomic model used for HD 45166 consists of 35 059 spectral lines from 2426 energy levels grouped in 617 super-levels of H, He, C, N, O, Si, Fe, and Ni, as shown in Table 1.

Table 1. Final atomic model used in the analysis of HD 45166. A single-level ion of one higher ionization stage is included for every species (e.g. C VI for carbon) and omitted below for brevity.

Ion	N_S	N_F	N_T
H I	30	20	435
He I	45	40	435
He II	30	22	233
C III	243	83	5513
C IV	64	60	1446
C V	107	43	2196
N III	287	57	344
N IV	60	34	331
N V	67	45	1554
O III	349	64	823
O IV	95	19	823
O V	34	34	118
O VI	13	13	59
Si IV	33	22	185
Si V	45	22	302
Fe IV	264	28	3889
Fe V	191	47	2342
Fe VI	433	44	8663
Fe VII	252	41	2734
Fe VIII	324	53	7305
Ni IV	200	36	2337
Ni V	183	46	1524

N_S = number of included superlevels; N_F = number of total energy levels; N_T = number of bound-bound transitions included for each ion.

4. Results: fundamental parameters of the qWR star

4.1. Effective temperature, luminosity and radius

The effective temperature was constrained using the relative strength of lines from different ionization stages of He, C, and N. The diagnostic lines used to obtain the He ionization structure were He I λ 5876, He I λ 6678, He II λ 4686, and He II λ 5411, while for the C ionization structure we used C III $\lambda\lambda$ 4647–4650–4651 and C IV $\lambda\lambda$ 5801–5812. The N ionization structure was obtained using the lines of N III λ 4097, N III λ 4634, N IV λ 4058, N IV $\lambda\lambda$ 7103–7109–7123, N V λ 4605, N V λ 4620, and N V λ 4945.

Figure 2 presents the fits to the diagnostic lines used to derive $T_{\rm eff}$ in this work. In particular, the relative strength between He I and He II lines requires $T_{\rm eff} > 47\,000$ K, otherwise the He I lines in the model become too strong compared to the observations, and the He II lines become too weak. The N ionization structure requires models with $T_{\rm eff} > 46\,000$ K in order to reproduce the ratio between the N III and N IV lines mentioned above. Reasonable fits to the N V lines are only achieved by models with $T_{\rm eff} > 50\,000$ K. The strongest C lines seen in the spectrum, namely C IV $\lambda\lambda$ 5801–5812, also require models with $T_{\rm eff} > 49\,000$ K to obtain reasonable fits to the observations. CMFGEN models with $T_{\rm eff} < 48\,000$ K produce too strong C III emission.

As can be seen in Fig. 2, the fits to the observed line spectrum are very sensitive to the effective temperature, and the use of three diagnostics in this temperature regime allowed us to constrain the effective temperature as $T_{\rm eff}(\tau = 2/3) = 50\,000 \pm 2000$ K. The temperature of the hydrostatic core was constrained to $T_\star(\tau = 100) = 70\,000 \pm 2000$ K and obtained through the use of a hydrostatic structure at depth. The hydrostatic structure is sensitive to the effective gravity and, hence, to the adopted stellar mass ($M = 4.2\ M_\odot$, Paper I).
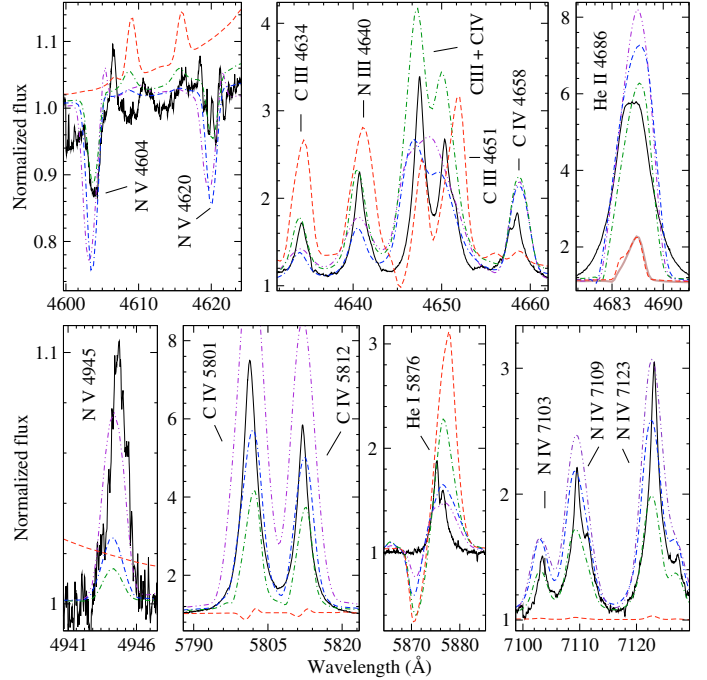

Fig. 2. Normalized spectrum of the qWR star in HD 45166 (black line) compared with spherical CMFGEN models with $T_{\rm eff} = 50\,000$ K (purple dash-double-dotted line), $T_{\rm eff} = 46\,000$ K (blue dot-double-dashed line), $T_{\rm eff} = 43\,000$ K (green dot-dashed line), and $T_{\rm eff} = 35\,000$ K (red dashed line). A model with the same parameters proposed by Willis & Burnley (2006) ($T_{\rm eff} = 35\,000$ K, $v_\infty = 1200$ km s^{-1}) produces fits similar to the original $T_{\rm eff} = 35\,000$ K model, and does not fit our optical data as well. For clarity, such a model is compared only to He II λ 4686 (brown thick line).

Even if it was not possible to reproduce lines corresponding to the observed ionization stages of He, C, and N using a unique best model with $T_{\rm eff} = 50\,000$ K, small changes in the range ± 2000 K were sufficient to adjust the discrepant lines (Fig. 2).

Models with other parameter regimes do not fit the optical spectrum of HD 45166 from 2004. For instance, increasing the terminal velocity of a model with $T_{\rm eff} = 35\,000$ K to $v_\infty = 1200$ km s^{-1} (i.e., the same model parameters of Willis & Burnley 2006) does not enhance the ionization degree of the wind and, therefore, does not fit the high-ionization optical lines. Such a high-terminal velocity model provides fits similar to the original $T_{\rm eff} = 35\,000$ K model with $v_\infty = 425$ km s^{-1} (Fig. 2).

The fundamental parameters of the qWR star obtained in this work, using tailored CMFGEN models to fit the continuum energy distribution *and* the optical spectrum, differ significantly from the previous published values. While we cannot exclude variability, the discrepancies between our results and previous works are at least partially explained by the inclusion of key physical ingredients in our analysis; namely, the inclusion of detailed non-LTE radiative transfer in the co-moving frame, full line blanketing, and use of a hydrostatic structure at depth, which allows simultaneous modeling of the photosphere and wind. However, since Willis & Burnley (2006) used the same radiative transfer code as ours, the aforementioned physical ingredients were presumably included in their modeling as well. The value of $T_{\rm eff}$ inferred by those authors (35 000 K) is 15 000 K lower than our determination, and this difference is puzzling.

In order to investigate this discrepancy in the values of $T_{\rm eff}$, we computed several CMFGEN models covering a broad range of effective temperatures to analyze the changes in the
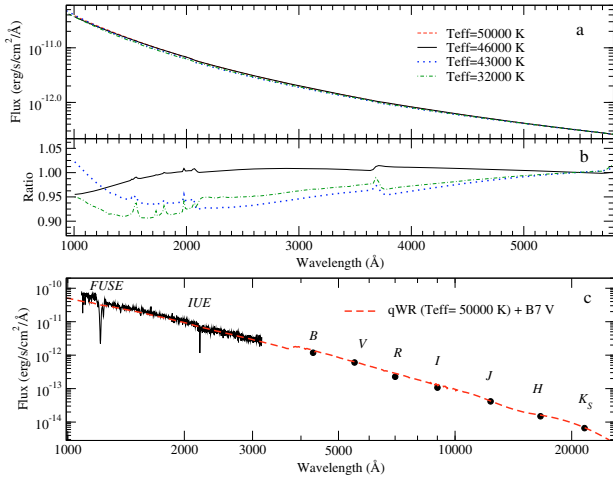
Fig. 3. **a)** Comparison between the continuum flux predicted by CMFGEN models for the qWR star in the range 32 000 K < T_{eff} < 50 000 K. All models were scaled to the observed de-reddened flux of the qWR star at 5500 Å (3.09×10^{-13} erg s^{-1} cm^{-2} Å^{-1}, see Fig. 1). Since the continuum slope is very weakly sensitive to the value of T_{eff} (see text for discussion), the models are basically superimposed on each other. **b)** Ratio between the continuum flux predicted by a CMFGEN model with a given T_{eff} and the continuum flux of the T_{eff} = 50 000 K CMFGEN model. **c)** Comparison between the total de-reddened observed flux of HD 45166 (black) and the flux predicted by the radiative-transfer model (red dashed line). The model shown here is composed of the sum of the continuum of the B7 V template from the companion (shown in Fig. 1) and the continuum of the best CMFGEN model for the qWR star.

Fig. 4. Velocity law (panel **a)**), density structure **b)**, electron density **c)**, and Rosseland optical depth **d)** of HD 45166 as a function of distance.

continuum, since this was the diagnostic of the effective temperature used by Willis & Burnley (2006). While the spectral lines are strongly sensitive to changes in T_{eff} (Fig. 2), we found that the continuum slope predicted by CMFGEN models in the range 32 000 K < T_{eff} < 50 000 K is almost insensitive to the adopted value of T_{eff} (Fig. 3a,b). Indeed, all such models provide good fits to the ultraviolet-to-near-infrared SED of HD 45166 (Fig. 3c). This is not surprising since such hot stars emit the bulk of their flux in the range 228–1000 Å. Similar results have long been found for other hot stars, such as Wolf-Rayet stars (Hillier 1987; Abbott & Conti 1987) and O-type stars (Martins & Plez 2006). We also computed models using a large value of the wind terminal velocity, as proposed by Willis & Burnley (2006), and found no noticeable changes in the continuum slope. This happens because the photosphere is located at rather low velocities (~30 km s^{-1}) in comparison with Wolf-Rayet stars, and changes in the velocity field have little impact on the continuum formation region and continuum spectrum shown in Fig. 3.

In the case of HD 45166, only small changes (of the order of 8% or less) are seen in the ultraviolet when comparing models in the range 32 000 K < T_{eff} < 50 000 K (Fig. 3b). Those changes are easily compensated by slightly adjusting other model parameters, such as the mass-loss rate, core radius, or reddening law. Even without changing any parameter those small changes in the ultraviolet flux tend to be masked by observational errors, since the 1σ error in the absolute photometry of the IUE and FUSE flux-calibrated spectrum is at least 5%. *Therefore, since models in the range* 32 000 K < T_{eff} < 50 000 K *provide good fits to the observed SED (Fig. 3c), we suggest that the technique of fitting the continuum is not suitable for constraining* T_{eff} *in the case of HD 45166, and very likely explains the discrepancy between the low* T_{eff} *suggested by Willis & Burnley (2006) and the value determined in this work.*
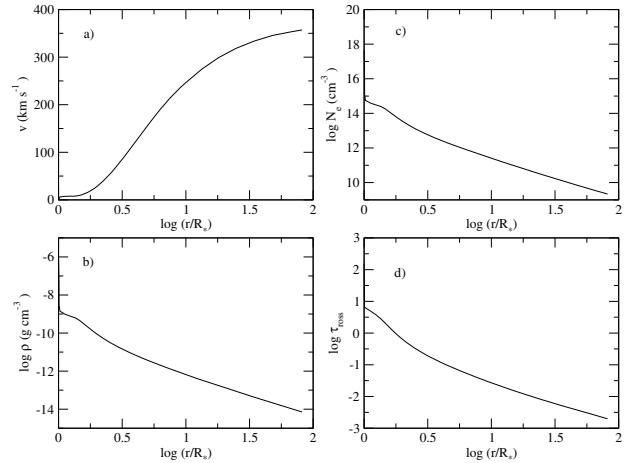
The stellar luminosity of the qWR star was obtained by matching the best-model flux, scaled to a distance of d = 1.3 kpc (Paper I), with the observed flux of HD 45166, de-reddened using $E(B - V)$ = 0.155. The photometry was taken from Willis et al. (1989), from Paper I, and references therein. We obtained a luminosity of $L_\star$ = 5650 $L_\odot$ (log($L/L_\odot$) = 3.75), with an error due to the uncertainties in the modeling, distance, reddening law, and photometry amounting to about 20% (0.08 dex). Figure 3c displays the de-reddened observed flux compared with the flux from the best CMFGEN model. We determined a luminosity significantly higher than that given by Willis & Burnley (2006), which is due to the significantly higher T_{eff} inferred by our detailed modeling of the spectral lines.

Combining the derived values of $T_\star$ and T_{eff} with $L_\star$, and using the Stefan-Boltzmann law, it is possible to determine the radius of the hydrostatic core of the qWR star as $R_\star(\tau = 100)$ = 0.51 $R_\odot$, and the radius of the photosphere (defined as τ = 2/3) as R_{phot} = 1.00 $R_\odot$.

4.2. The mass-loss rate

We derived $\dot{M}$ = 2.2 × 10^{-7} $M_\odot$ yr^{-1} in order to reproduce the strength of the spectral lines present in the optical spectrum taken in 2004. We also obtained a volume filling factor of f = 0.5, using the electron-scattering wings of He II λ 4686 and C IV $\lambda\lambda$ 5801–5812 as diagnostics. However, the electron scattering wings are weak, and we cannot rule out the presence of an unclumped wind (f = 1), with $\dot{M}$ = 3.1 × 10^{-7} $M_\odot$ yr^{-1}. The value of the clumped $\dot{M}$ derived in this work agrees with the proposed value given by Willis & Burnley (2006), while the value of the unclumped $\dot{M}$ derived here is 50% higher than the value obtained by them.

Using the value of the mass-loss rate combined with the velocity law derived in Sect. 4.3 and the equation of mass continuity, we obtain the wind density structure shown in Fig. 4.

4.3. Wind terminal velocity and momentum transfer

From our optical spectrum we did not detect velocities above +550 km s^{-1} for the He II λ 4686 line (see Paper I). For the He I λ 5876 line, however, the maximum velocity observed is much lower (280 km s^{-1}). For the C IV $\lambda\lambda$ 5801–5812 lines, a strong emission exists at low velocity, while weak emission can be seen extending up to 600 km s^{-1}. From the model fit to

He II λ 4686 and He II+Hα λ 6560, we obtained a wind terminal velocity of v_∞ = 425 ± 50 km s^{-1}. The value of the acceleration parameter β was set to 4.0 in order to reproduce the relative strength among the He II lines of the Pickering series. In particular, it was impossible to reproduce the high-order He II lines of the Pickering series using lower values of β. The velocity law obtained is shown in Fig. 4 (panel a).

The value of v_∞ derived from the optical lines in this work is ~3 times lower than what was derived from the observations of UV resonance lines (v_∞ ~ 1200 km s^{-1}, Willis & Stickland 1983). One possible explanation for the different values of v_∞ derived from the UV and optical spectrum is the presence of a latitude-dependent wind, with a higher wind terminal velocity in the polar direction, and a slower equatorial wind. This possibility is further explored in Sect. 5.

From the optical lines, we obtained that the efficiency of the momentum transfer from the radiation to the gas (η) is much smaller in HD 45166 than in WR stars. The momentum of the gas is $\dot{M}v_\infty$, while the momentum of the radiation is $L_\star$/c. The ratio between the two momenta for WN stars is $\eta \simeq 2.8$ (Crowther 2007), while for HD 45166 we obtain η = 0.74 . As a consequence, the wind driven by radiation pressure is less efficient in HD 45166 than in WR stars, which can explain the low ratio $v_\infty/v_{\rm esc}$ found for HD 45166. For instance, O-type stars in about the same temperature range have $v_\infty/v_{\rm esc}$ = 2.6 (Lamers et al. 1995), while WR stars have $1.5 < v_\infty/v_{\rm esc} < 4$ (Lamers & Cassinelli 1999). However, in HD 45166, $v_{\rm esc} = 1320$ km s^{-1}, $v_\infty = 425$ km s^{-1}, and therefore $v_\infty/v_{\rm esc}$ = 0.32, i.e., at least 5 times lower than in typical WRs. This is difficult to achieve for a normal wind, since it requires a fine balance between gravity and line forces. The presence of the close B7 V companion, fast rotation, and/or deviations from a spherical wind could explain such an extremely low ratio. Using $v_\infty = 1200$ km s^{-1} derived from the UV lines (Willis & Stickland 1983), the ratio $v_\infty/v_{\rm esc}$ is increased to ~1, becoming closer to the value for O-type and WR stars.

4.4. Surface abundances

The surface abundances obtained with CMFGEN are summarized in Table 3. The helium abundance was determined adjusting the helium content in the models to match the observed intensity of He II λ 4686, He II λ 5411. and the blend of He II + Hα λ 6560. The value obtained is N(H)/N(He) = 2.0, which corresponds to about 2.3 times the solar abundance of He (hereafter we used the solar abundance values from Cox 2000, and references therein).

The model calculations constrained C and N abundances that are significantly higher than the abundances of O and Si. The abundances of HD 45166 are in fact quite anomalous when compared to solar values, or to the values found in central stars of planetary nebulae or Wolf-Rayet stars (see Table 4). This emphasizes the peculiar nature of HD 45166.

The chemical abundances must be analyzed in view of the evolutionary status of both stars in the HD 45166 system, which is beyond the scope of this paper. Such a detailed analysis will be the subject of a forthcoming Paper III. We anticipate that the star is likely an exposed He core (Marco et al. 2007), which is probably related to the presence of the close secondary. We suggest that He burning is currently going on in the nucleus, producing carbon, and, thus, explaining the He and C overabundance. As the star still has an H-rich envelope, there certainly is a shell burning H through the CNO-cycle, enhancing the N content. As
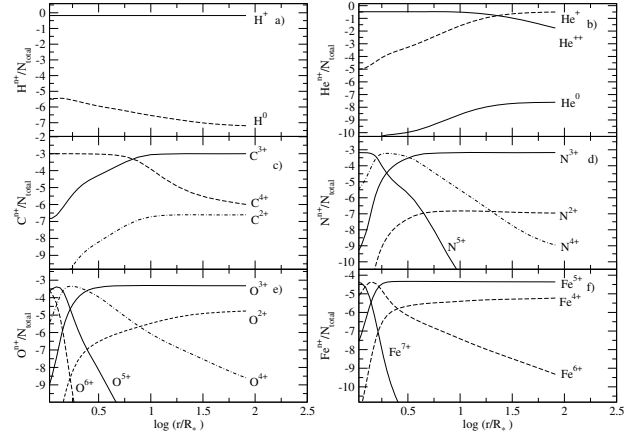
Fig. 5. Ionization fractions of HD 45166 as a function of distance, derived from the spherical CMFGEN models of the most abundant ions in the wind of the qWR star. The ionization fractions are normalized by the total number of ions.

can be seen in Table 3, heavier elements such as Si, Ni and Fe have solar abundances.

4.5. The ionization structure of the wind

Figure 5 presents the ionization structure of the wind of the qWR star determined using the spherical CMFGEN model. H is fully ionized along the whole wind, but the He, C, and Fe ionization structures are more stratified, with He^{2+} and C^{4+} being more abundant in the photosphere and in the inner wind, while He$^+$ and C^{3+} dominating at distances greater than about 10 $R_\star$. This also explains the high sensitiveness of the He, C, and Fe lines on the model parameters. On the other hand, the O and N ionization structures are dominated respectively by O^{3+} and N^{3+} ions in most of the wind – O^{4+} and N^{4+} are present in significant fractions only at distances of less than ~1.5 $R_\star$.

5. Presence of a latitude-dependent wind

5.1. Observational evidence from the line profiles

The spherical models obtained with CMFGEN reproduce the strength of most of the emission lines, provide a superb fit to the continuum of the qWR, and a reasonable fit to the spectral lines, considering the complex physical nature of HD 45166 (see Figs. 6 and 7). However, some discrepancies are present when comparing the line profiles predicted by the best spherical model with observations (Fig. 2). These discrepancies might provide key insights into the validity of the model assumptions.

As already mentioned in Paper I, the hydrogen and helium line profiles are clearly different from the CNO lines profiles. The later can be very well fitted by Lorentzian profiles, while He II λ 4686 and the other He II lines are better fitted by a Voigt/Gaussian profile. The full widths at half maximum (*FWHM*) are also significantly different between the two groups of lines.

Insights into the physical interpretation of the line profiles from different species can be obtained with the best CMFGEN model obtained in Sect. 4, which assumes a spherical wind with a monotonic velocity law. We present in Fig. 8 the line formation regions for the most important diagnostic lines present in the spectrum of HD 45166. The inner layers correspond to the formation region of higher-ionization lines such as N V and
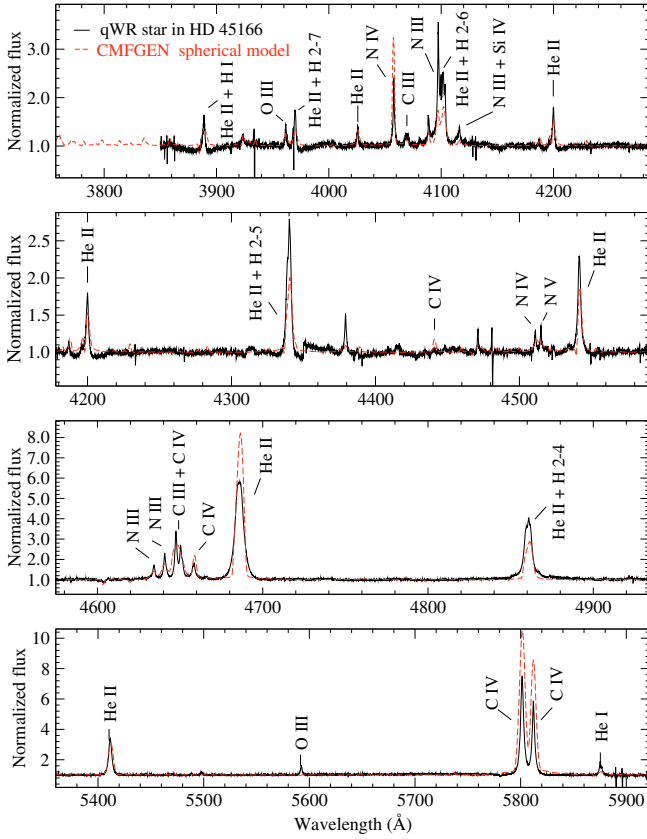
Fig. 6. Comparison between the line profiles predicted by the best CMFGEN spherical model with the observations of HD 45166, in the spectral region 3850–5950 Å. The strongest spectral lines used in the analysis are identified.

C IV, while the outer layers correspond to the formation region of lower-ionization lines such as N III, C III, and He I. As can be seen in the CMFGEN model spectrum displayed in Figs. 2, 6, and 7, the higher-ionization lines are predicted to be narrower than the lines of lower ionization. In addition, recombination lines such as those from H and He are emitted in an extended region of the wind and, therefore, should be broader than N IV and N V lines, for instance.

Indeed, the N IV and N V lines are narrow in the observations, while the He II lines are broad, and both are well reproduced by the spherical CMFGEN models. However, the lower-ionization lines, such as C III, N III, and He I, are surprisingly narrow in the observations – much narrower than the He II and C IV lines.

We examined the effects of changing one or more physical parameters to improve the fit of the lower ionization lines, running a large number of additional CMFGEN models. None of them improved the fit to those line profiles, i.e., they did not provide narrower lower-ionization lines. The only way to change the width of those lines using a spherical model is by using a much lower terminal velocity of $\sim$70 km s^{-1}, which obviously did not fit the other strong spectral lines. Moreover, it would be hard to explain the origin of such a very low wind terminal velocity in a very hot star ($T_{\mathrm{eff}} = 50\,000$ K). *In summary, a spherical symmetric wind cannot reproduce the profile of the lower-ionization lines.*

Therefore, we propose the presence of a latitude-dependent wind in the qWR star to explain the narrow profiles observed in the N III, C III, and He I lines. Using the code outlined in Sect. 5.2, we examine the effects due to changes in the wind
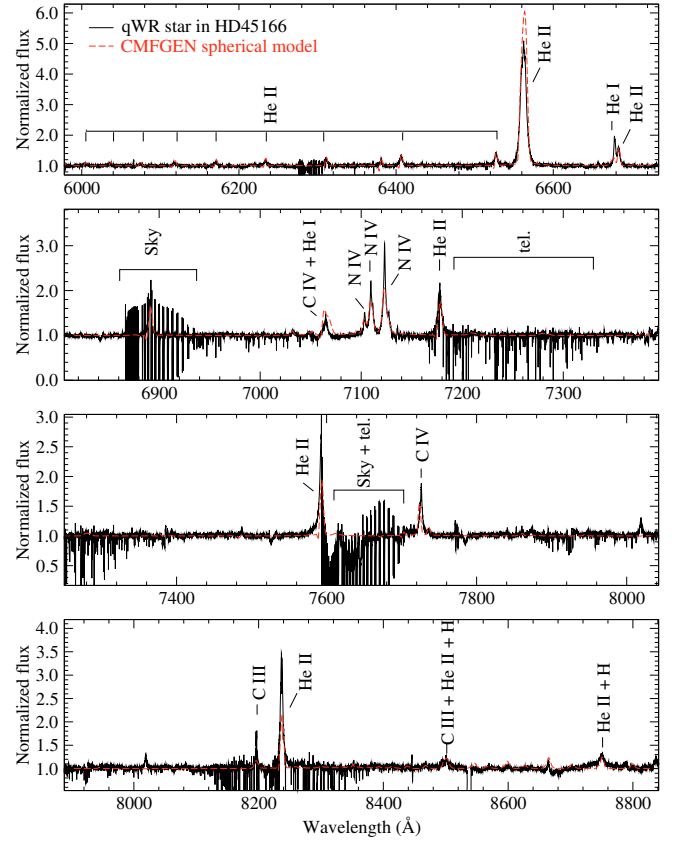
Fig. 7. Same as Fig. 6, but for the spectral region of 6000–8800 Å.
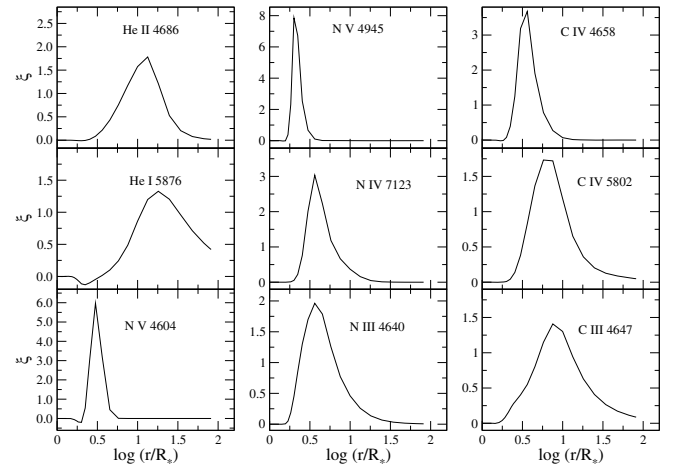
Fig. 8. Line formation region for the strongest lines of HD 45166 used in the spectroscopic analysis. For each panel the quantity ξ is displayed, which is related to the *EW* of the line (following Hillier 1989) as $EW = \int_{R_\star}^{\infty} \xi(r)\mathrm{d}(\log r)$.

density and terminal velocity as a function of the stellar latitude, and present the results in Sect. 5.3.

5.2. The 2D calculation of the emerging spectrum

Ideally, solving a full set of 2D radiative transfer and statistical equilibrium equations would be required to analyze a non-spherical stellar wind as in HD 45166. However, this is currently impossible taking into account all the relevant physical processes, full line blanketing, and the degree of detail achieved

by spherically-symmetric codes such as CMFGEN. The large parameter space to be explored in 2D models, and the huge amount of computational effort demanded, do not allow one to perform a self-consistent 2D analysis of very complex objects such as HD 45166.

Nevertheless, significant progress has been achieved in developing full 2D radiative transfer codes (Zsargó et al. 2006; Georgiev et al. 2006), which can be applied to HD 45166 in future works. Therefore, it is desirable to explore the parameter space suitable for HD 45166, using justified assumptions to make the computation of the observed spectrum in 2D geometry a tractable problem.

In this work we used a recently-developed modification in CMFGEN (Busche & Hillier 2005) to compute the spectrum in 2D geometry. We refer the reader to that paper for further details about the code, whose main characteristics are outlined below.

With the Busche & Hillier (2005) code, it is possible to examine the effects of a density enhancement and changes in the velocity field of the wind as a function of latitude. The code uses as input the ionization structure, energy-level populations, temperature structure, and radiation field in the co-moving frame, as calculated by the original, spherically-symmetric CMFGEN model. Using CMF_FLUX (Hillier & Miller 1998; Busche & Hillier 2005), the emissivities, opacities, and specific intensity J are calculated from the spherically-symmetric model.

A density enhancement and wind terminal velocity variation can then be implemented using an arbitrary latitude-dependent density/wind terminal velocity distribution. We examined the effects due to oblate and prolate density parameterizations, which have the form

$$\rho_{2D} \propto \rho_{1D} \left(1 \mp a \cdot \cos^b \theta\right), \tag{2}$$

where θ is the latitude angle ($0° =$ pole, $90° =$ equator). The changes in the wind terminal velocity as a function of latitude were parameterized using three parameters (VB1, VB2, and VB3),

$$v(r)_{2D}/v(r)_{1D} = VB1 + \left(VB2 \, |\cos(\theta)^{VB3}|\right). \tag{3}$$

We assumed in this work a scaling law according to which the 2D model has the same mass-loss rate as the spherically-symmetric 1D model.

After computing the density changes and velocity field variations, the 2D source function, emissivity, and opacity are calculated, assuming that these quantities depend only on the new values of the scaled density. Consistent scaling laws are used for different processes (e.g. density-squared scaling for free-free and bound-free transitions, and linear-density scaling for electron scattering).

In the final step, the code computes the spectrum in the observer's frame, which can then be compared with the observations.

5.3. Model fits, results, and constraints on the wind asymmetry

The 2D model spectra were computed following the physical parameters of the best CMFGEN spherical model shown in Tables 2 and 3. We varied the density enhancement and velocity field as a function of latitude, and Table 5 summarizes the properties of the 2D models. Figure 9 shows the latitudinal changes in the density enhancement (normalized to the best spherical

Table 2. Fundamental parameters derived for the qWR star in HD 45166.

Parameter	Value
$\log (L_\star/L_\odot)$	3.75 ± 0.08
$T_\star$ (K)	$70\,000 \pm 2000$
$T_{\rm eff}$ (K)	$50\,000 \pm 2000$
$R_\star/R_\odot$ ($\tau = 100$)	0.51
$R_{\rm phot}/R_\odot$ ($\tau = 0.67$)	1.00
$\dot{M}$ ($M_\odot$ yr^{-1})	2.2×10^{-7}
v_∞ (km s^{-1})	425
β	4.0
f	0.5
$v_{\rm c}$ (km s^{-1})	100

Table 3. Surface chemical abundances of HD 45166.

| Species	Number fraction	Mass fraction	$Z/Z_\odot$
H	2.0	3.3×10^{-1}	0.46
He	1.0	6.5×10^{-1}	2.34
C	3.0×10^{-3}	5.9×10^{-3}	1.93
N	2.0×10^{-3}	4.6×10^{-3}	4.17
O	1.5×10^{-3}	3.9×10^{-3}	0.41
Si	6.8×10^{-5}	3.6×10^{-4}	1.00
Fe	1.3×10^{-4}	1.4×10^{-3}	1.00
Ni	6.6×10^{-6}	7.3×10^{-5}	1.00

model) for the different models. We analyzed the effects of latitudinal changes in the density by comparing the 2D model spectra with the observed line profile of He I λ 5876, which is very sensitive to latitudinal changes, and has the most deviating line profile in the spherical model. This line is also isolated, minimizing the errors due to blending. Similar effects are seen in other low ionization lines of He I, C III, and N III.

Figure 10 displays the observed spectrum of the qWR star around 5800 Å compared with different 2D model spectra, labeled as in Table 5. All models were computed for a viewing angle of $i = 0.77°$ (Paper I), and the best spherical CMFGEN model is overplotted on each panel for comparison.

The immediate conclusion from Fig. 10 is that the wind of the qWR star cannot be prolate (model 2), as the fit to the He I line becomes even worse than the fit from the spherical model. This happens because, as the system is viewed pole-on, a prolate wind implies an enhanced density in the polar regions compared to the spherical model, producing stronger P-Cygni absorption and stronger emission at high velocities – exactly what is seen in the spectrum of model 2.

We can also rule out that the narrow He I line profile is only due to changes in the wind terminal velocity as a function of latitude, as is illustrated by model 8. This model assumes a slow equatorial wind ($v_\infty = 70$ km s^{-1}) and a fast polar wind ($v_\infty = 700$ km s^{-1}). Although the fit to the emission component is improved, the P-Cygni absorption is still very strong, since the density enhancement has not been changed as a function of latitude.

Therefore, it seems clear that a density enhancement in the equatorial region is required to reproduce the observed emission, and a density depletion along the polar regions is required to reproduce the lack of a P-Cygni absorption in He I λ 5876. The minimum density contrast equator:pole that fits the observations is 8:1, but we cannot rule out larger enhancements, such as 16:1. However, we have to keep in mind that larger enhancements will likely change the ionization structure of the wind as a function of
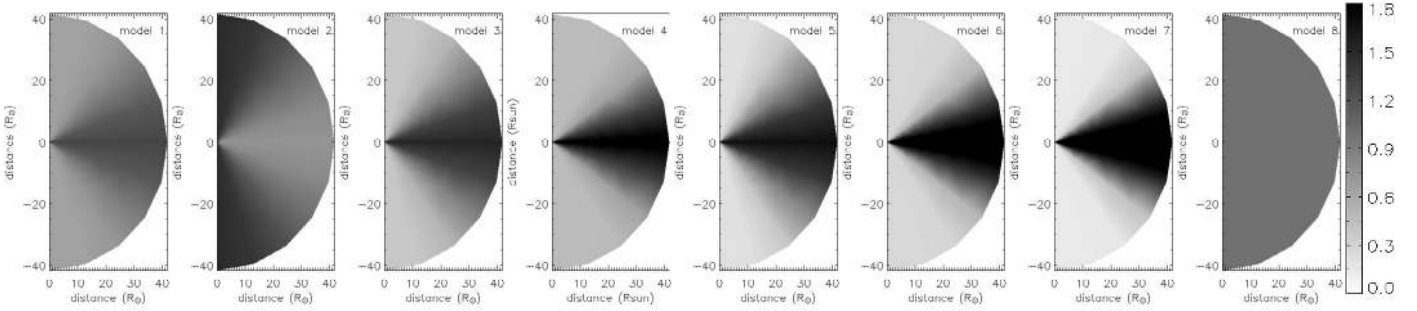
Fig. 9. Density contrast of the HD 45166 models with latitude-dependent density distributions (normalized to the density distribution of the spherical model), as a function of latitude. Each model is labeled as in Table 5; model 9 has the same density distribution as model 4, and is not shown. The equator of the star is at $[x, 0]$, while the pole is located at $[0, y]$. The colorbar in the right has a linear color scale, which we adopted the same for all models, to highlight the different density variations as a function of latitude. The maximum value in the colorbar is 1.8, which corresponds to the maximum value found in model 5.

Table 4. Abundance ratios (in number) of HD 45166 compared to different object classes.

| Object	He/H	C/N	O/N	Reference
HD 45166	0.5	1.5	0.75	1
Sun	0.085	8.6	7.2	2
PN I	0.14	0.7–3	1.2	3
PN II	0.11	1.4–9	3.5	3
WNL	H-free	0.04	…	4
WNE	H-free	0.02	…	4
WNEw	1.5	0.005	0.05	4

References: (1) this work; (2) Grevesse et al. (2007); (3) Peimbert (1990); (4) Crowther (2007).

Table 5. Summary of the parameters used to compute the spectrum in 2D geometry using the Busche & Hillier (2005) code. Note that the density contrast between equator and pole is given by $1 + a$ for oblate models, and $1/(1 + a)$ for prolate models.

Model	Density profile	a	b	Velocity changes?	$VB1$	$VB2$	$VB3$
1	oblate	1	2	no	…	…	…
2	prolate	1	2	no	…	…	…
3	oblate	3	2	no	…	…	…
4	oblate	3	5	no	…	…	…
5	oblate	7	2	no	…	…	…
6	oblate	7	5	no	…	…	…
7	oblate	15	2	no	…	…	…
8	none	…	…	yes	0.2	0.8	4
9	oblate	3	2	yes	0.8	2.2	4

latitude, which is not accounted for in the current calculations. The parameter b, which describes how fast the density changes from equator to pole, is difficult to constrain. A model with a density contrast of 8:1 and $b = 5$ (model 6) produces almost the same He I line profile as a model with a density contrast 16:1 and $b = 2$ (model 7).

We also examined changes due to both an oblate density enhancement and changes in the wind terminal velocity as a function of latitude. However, there is no clear evidence from the fits to the optical lines that a higher velocity polar wind is required, although it cannot be ruled out. If there is such change in the wind terminal velocity, the minimum density contrast from equator to pole is reduced to 4:1 (see model 9 in Fig. 10). Clearly, the largest effect of a fast polar wind would be seen in the ultraviolet resonance lines. However, we refrained from analyzing the
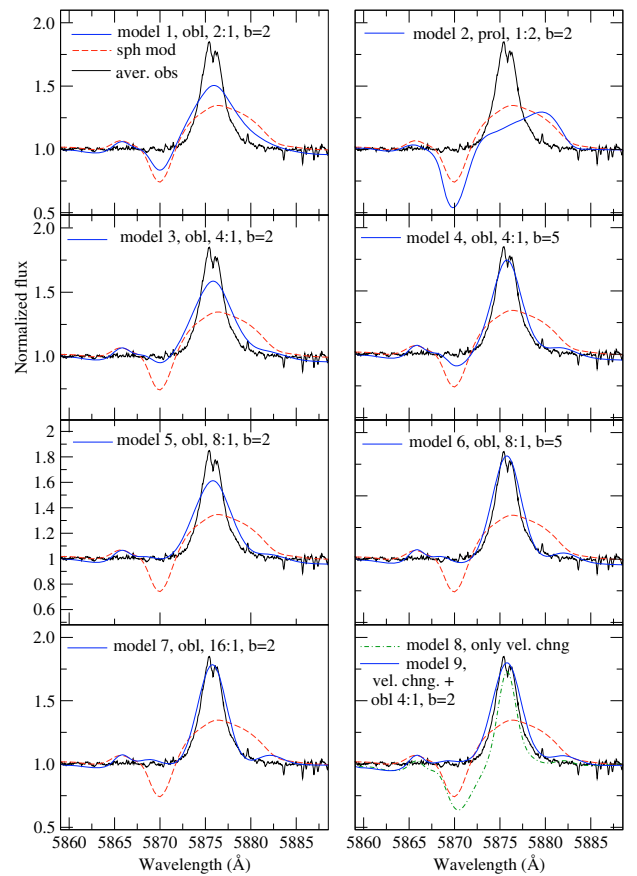
Fig. 10. Comparison between the line profiles computed with the 2D code of Busche & Hillier (2005) (blue line) with the observations of HD 45166 around He I λ 5876 (black line). For each panel the models are labelled as in Table 5, followed by the density contrast equator:pole, and the parameter b. The best spherical-symmetric CMFGEN model (red dashed line) is repeated in each panel for comparison (see text for further details). The weak dip in the observed He I λ 5876 line profile is likely due to incomplete subtraction of the secondary star spectrum.

archival IUE data simultaneously with our optical dataset due to the high variability of HD 45166 and the long time lag of 15–20 years between the IUE ultraviolet observations and our optical data. We acknowledge the wealth of information and the fundamental importance of the UV observations to constrain the

nature of HD 45166, and a forthcoming paper will be devoted to a detailed analysis of the UV spectrum.

There is clear observational evidence of a high velocity outflow in HD 45166 through the analysis of the discrete absorption components (DAC) in the resonance lines of HD 45166 (Willis et al. 1989). However, it is also clear that marked variability is present, and at some epochs the UV resonance lines (e.g. C IV $\lambda\lambda$ 1548–1550) do not show any high velocity absorption component (Willis et al. 1989). Two questions need to be answered:

1. Does the velocity of the DACs reflect the true wind terminal velocity along the polar direction? While in OB stars the maximum velocity of the DACs tend to mimic the wind terminal velocity (e.g. Prinja & Howarth 1986), further work is required to establish whether the same holds for HD 45166;
2. Do the DACs reflect an intrinsic property of the qWR and its steady wind or is the presence of a close companion somehow related to the variability seen in the UV lines?

Contemporaneous ultraviolet and optical spectroscopy are required to answer these questions, and we will come back to them in Paper III.

In this work we have not considered latitudinal changes in the wind ionization structure derived from the spherical CMFGEN modeling (Sect. 4.5), which likely occur in the case of large density changes. The inclusion of this effect would likely reduce the density contrast determined from our analysis, but the main conclusions reached in this work would remain valid. This is because *a density contrast is needed to change the ionization structure of the wind*, since the radiation field of the B7 V companion is too weak. The exact treatment of the effects of the latitudinal changes in the ionization structure of the wind is beyond the scope of this paper.

6. The temporal variance spectrum

We performed a temporal variance spectrum (TVS) analysis in order to study the characteristics of the emission line profiles. In this procedure, the temporal variance is calculated, for each wavelength pixel, from the residuals of the continuum normalized spectra and the average spectrum. For further details and discussion on the TVS method, see Fullerton et al. (1996).

We calculated the TVS for the strongest spectral lines, such as He II λ 4686, He I λ 5876, and C IV $\lambda\lambda$ 5801–5811 (Fig. 11). The TVS contain a large amount of information that, in spite of not being always immediately interpretable, certainly can be helpful in understanding the wind structure. As well as in the line profiles, the TVS is quite different when we compare, for instance, He II λ 4686 and C IV $\lambda\lambda$ 5801–5812. In the wings of He II λ 4686, the TVS is close to a Lorentzian profile. At lower velocities, however, the TVS profile of the line deviates more and more from a Lorentzian profile until it reaches a local minimum. Assuming that the Lorentzian profile is a signature of optically-thin line emission, the wind seems to become transparent for He II line photons at velocities greater than 270 km s^{-1}. The corresponding radius is $r = 10\,R_\star$, according to the velocity law determined using the best CMFGEN model. The CMFGEN model itself predicts that τ(He II4686) < 1 for $r > 15\,R_\star$ (see Fig. 4).

On the other hand, the TVS of the He I λ 5876 line presents a peculiar behavior. While the intensity profile is asymmetric to the red, the TVS profile is asymmetric to the blue. This discrepancy is quite strong and its interpretation is not simple. The
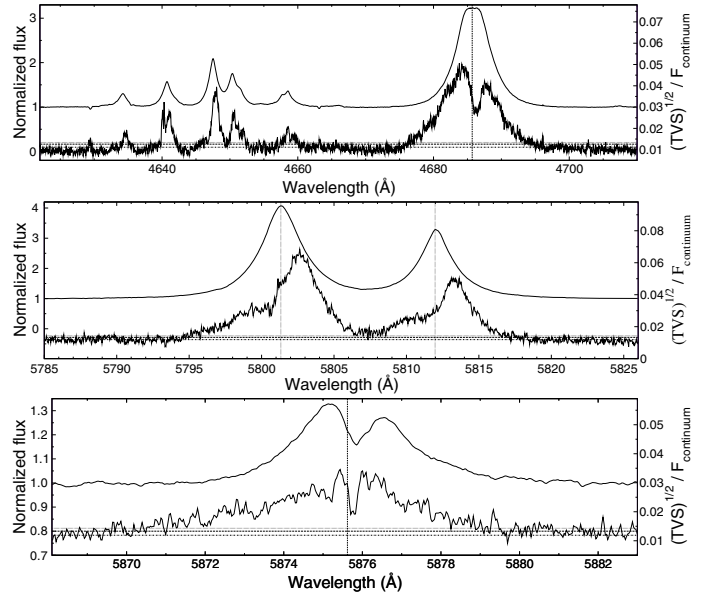
Fig. 11. Average intensity spectrum and TVS of HD 45166 for He II λ 4686 (*upper panel*), C IV $\lambda\lambda$ 5801–5812 (*middle*), and He I λ 5876 (*bottom*). The TVS statistical threshold significance of $p = 1\%$, 5%, and 30% are represented by the dotted, dashed, and dot-dashed horizontal lines, respectively. The vertical dotted lines mark the position of the zero velocity for the relevant line presented in each panel. See text for details.

stronger H lines of Hα and Hβ are blended with the He II lines and, therefore, their profile and interpretation is more complex.

A noticeable feature in the TVS profiles is the presence of a central dip in the He II and He I lines. In the case of He II, this dip is centered at a velocity of $+35.3 \pm 0.6$ km s^{-1}. We do not have an interpretation for this velocity. In the TVS profile of He I λ 5876, however, the dip is at a different velocity of $+4.1 \pm 0.1$ km s^{-1}, which is consistent with the systemic velocity of $+4.5 \pm 0.2$ km s^{-1} (Paper I). On the other hand, in the intensity spectrum of He I λ 5876, the absorption is centered at $+9.2 \pm 0.3$ km s^{-1}. Interestingly, this is remarkably similar to the photospheric velocity found for the absorption lines of the secondary star. Therefore, we suggest that such a dip in the TVS of He I λ 5876 is due to the orbital motion of the secondary star.

Most of the intensity line profiles present in the spectrum of HD 45166 are quite symmetric. The lines of C IV $\lambda\lambda$ 5801–5811, for instance, are very well fitted by symmetrical Lorentzian profiles, as already mentioned in Paper I. However, in the TVS the asymmetries are much more evident. For the lines of N III $\lambda\lambda$ 4634–4640, C III $\lambda\lambda$ 4647–4650 and C IV λ 4658, as well as for C IV $\lambda\lambda$ 5801–5812 (see Fig. 11), the TVS profiles are very different from the intensity profiles of the respective lines as well as from the TVS of the He II λ 4686 line. While in the TVS of the latter the blue wing is 30% more intense than the red wing, in the lines of C and N the opposite happens. For instance, in the TVS of C IV $\lambda\lambda$ 5801–5812, the red wings are 3 times stronger than the blue wings (see Fig. 11). We interpret this phenomenon as evidence for temporal changes in the gas density of the equatorial wind region. This produces a variable optical depth (due to absorption or electron scattering) and primarily affects the red part of the profile, which is formed in the receding side of the wind. The nature of the variability in the gas density is not clear, and a detailed interpretation is beyond the scope of this paper. Two possible interpretations are variability in the (equatorial) mass-loss rate, or debris from a hypothetical,

Table 6. σ/I for the strongest lines present in HD 45166. Both σ and I were measured at the centroid of the lines.

Ion	Line	σ/I (%)
H I + He II	4861	2.0
H I + He II	6563	2.2
He I	5876	2.6
He I	6678	2.1
He II	4541	1.6
He II	4686	1.5
He II	6527	1.4
He II	6683	1.3
C IV	5801	1.6
C IV	5812	1.5
C III	4647	1.9
N III	4510	1.1
N III	4640	1.9

variable mass transfer from the secondary star. The latter hypothesis will be examined in Paper III.

A characteristic indicator of each line is the ratio between its variance and the intensity, σ/I. Table 6 presents this ratio for the strongest lines of HD 45166[1]. It is interesting to notice that He I lines have the highest σ/I values (2.6%), followed by H I + He II lines, which are estimated to be about 2.5%. The higher variability of low ionization lines can be interpreted in the context of a Wind Compression Zone (WCZ) scenario (Ignace et al. 1996), in which a lower ionization region is produced at the equator of the system (see Sect. 7.2). Variability in the WCZ may cause a higher σ/I ratio for the He I and H I lines when compared to the higher ionization lines of He II or C IV. It is not clear whether the same scenario can explain the variability detected in the photospheric UV lines of Fe V, He II, and N IV (Willis et al. 1989).

7. Discussion

7.1. Gravitational redshift and the line formation regions

The gravitational redshift is measurable in the CNO emission lines of HD 45166 (see Paper I). The CNO III lines have an average radial velocity of 5.0 ± 0.8 km s^{-1} (Table 7). This is compatible with the systemic velocity $\gamma = 4.5 \pm 0.2$ km s^{-1} (Paper I). However, the N IV–N V lines have an average radial velocity of 8.3 ± 1.2 km s^{-1} (Table 7). These higher-ionization lines should be emitted in the wind inner layers and, therefore, should be redshifted when compared to the lines of lower ionization. Indeed, the observed velocity shift of those more ionized species, compared to the less ionized ones, is 3.3 ± 1.2 km s^{-1}. This means that, taking the systemic velocity as a reference, the CNO III lines should be emitted at distances larger than $\sim 10\,R_\star$, assuming the velocity law derived in Sect. 4.3, and $M_{\mathrm{qWR}} = 4.2\,M_\odot$ (Paper I). Interestingly, those distances are comparable to the size of the Roche lobe of the qWR star. In contrast, the gravitational redshift of the N IV–N V lines indicates that they should be emitted close to the hot star, at distances of the order of $1.5-2.0\,R_\star$.

---

[1] The telluric lines in absorption have a much higher TVS in our data (28%), and, therefore, those lines can be easily identified and differentiated from the stellar lines. On the other hand, the interstellar lines should not appear in the spectrum of the TVS. The TVS can be a useful method to distinguish between the several types of lines present in a rich emission and absorption line spectrum such as in HD 45166.
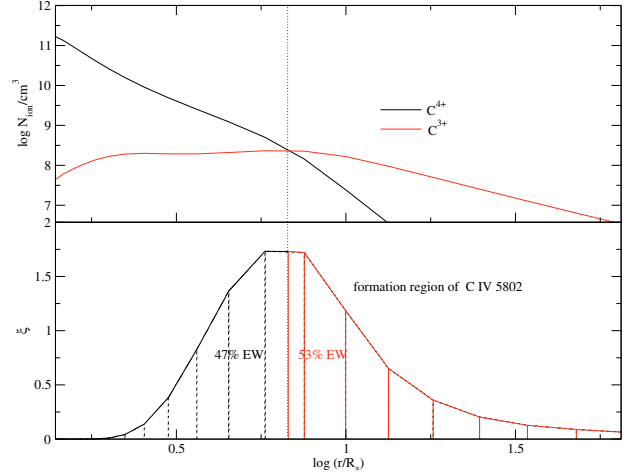
Fig. 12. Upper panel: radial density profile of the C^{3+} and C^{4+} ions along the wind of HD 45166. *Lower panel*: line formation region of C IV $\lambda\lambda$ 5801. The quantity ξ is related to the *EW* of the line (following Hillier 1989) as $EW = \int_{R_\star}^{\infty} \xi(r)\mathrm{d}(\log r)$.

Table 7. Average *FHWM* and radial velocity of the spectral lines for the most abundant ions present in HD 45166.

Ion	$\langle FWHM \rangle$ (km s^{-1})	$\langle v_r \rangle$ (km s^{-1})
C IV	142 ± 19	4.4 ± 0.4
C III	91 ± 6	5.4 ± 1.5
N V	79 ± 20	7.3 ± 1.6
N IV	82 ± 11	8.6 ± 1.5
N III	96 ± 4	4.0 ± 1.1
O III	113 ± 9	5.0 ± 1.6
$\langle$CNO III$\rangle$	102 ± 4	5.0 ± 0.8
$\langle$N V + N IV$\rangle$	78 ± 10	8.3 ± 1.2

The above values are in reasonable agreement with the line formation regions presented in Fig. 8, taking into account that the lines actually form in an extended wind region. One should also consider that the emission lines can be a result of pure recombination (e.g. C IV λ 4658) or, at least partially, due to continuum fluorescence (e.g. C IV $\lambda\lambda$ 5801–5812). This is shown in Fig. 12, where the line formation region of C IV $\lambda\lambda$ 5801 is compared to the radial variation of the density of C^{3+} and C^{4+} ions. It can be seen that roughly 50% of the line emission comes from an inner region where the dominant ionization stage of carbon is C^{4+}, suggesting that the line is formed by recombination. However, a significant fraction of the line formation occurs under very low C^{4+} density conditions, making it very unlikely that recombination is the main mechanism of line emission in those regions. Instead, we suggest that the line is emitted due to continuum fluorescence of the C^{3+} ions.

This discussion illustrates that the physical conditions found in HD 45166 are far too complex to be properly described by a spherical wind model. Therefore, understanding the line formation processes and determining the line formation regions provide invaluable information on the nature of HD 45166.

7.2. Rotation, wind asymmetry, and formation of a wind compression zone

Depending on the rotational velocity of the star and on the velocity law of the wind, a wind compression disc (WCD, Bjorkman & Cassinelli 1993), or a wind compression zone (WCZ,

Ignace et al. 1996), can be formed. The most fundamental parameter to consider is the ratio of the rotational velocity of the star (v_{rot}) to the critical break-up velocity (v_{crit}). Since HD 45166 is seen almost pole-on ($i = 0.77°$, Paper I), it is impossible to detect the rotational broadening of lines formed close to the photosphere, and to further determine the rotational velocity using the Busche & Hillier (2005) code, similar to what has been done, for instance, for the luminous blue variable AG Carinae (Groh et al. 2006).

Nevertheless, the effects due to the rotation of HD 45166 can be quantified in terms of the ratio of the critical period for breakup (P_{crit}) to the rotational period (P_{rot}),

$$v_{rot}/v_{crit} = P_{crit}/P_{rot}, \qquad (4)$$

where $v_{crit} = (GM_\star/R_\star)^{1/2}$. For values of v_{rot}/v_{crit} close to 1 a WCD can be formed (Bjorkman & Cassinelli 1993), while for moderate rotational velocities a WCZ can be produced (Ignace et al. 1996).

Using the stellar parameters determined for HD 45166 (see Sect. 4), we have $P_{crit} \simeq 1.0$ h. Therefore, unless the rotational period is close to 1 h, the rotation is too slow to cause the formation of a WCD. However, the formation of a WCZ may still be possible, and might explain the degree of asymmetry detected in the wind of HD 45166 (see Sect. 5). In Paper III we will show evidence of a period of 2.4 h, which might be related to rotational modulation.

The difference between the two scenarios outlined above is that, in the case of a WCD, the formation of a stationary shock heats up the disc, and compresses it to a thin sheet with high density (Bjorkman & Cassinelli 1993). In the case of a WCZ, this shock does not exist and the compression area is much thicker and less dense (Ignace et al. 1996). While for a WCD the ratio between equatorial and polar density is of the order of ∼1000, for a WCZ with the parameters of HD 45166 this ratio is ∼5−10. The value of the density contrast derived from our 2D modeling is 4–8 (see Sect. 5), which is of the same order as predicted by the WCZ scenario.

In addition, in the case of a WCD, the shock formed in the equatorial region should be hot enough to be detected in soft X-rays. However, HD 45166 was not detected by the *ROSAT* X-ray satellite. Superionization due to X-rays (Bjorkman & Cassinelli 1993) should also produce enhanced N v and O vi emission near the equator, which is not observed. In contrast, on the equator there is enhanced emission of low ionization species such as He I lines (see Sect. 5), which argues against the presence of a WCD.

However, there are at least two caveats which might change the WCZ/WCD scenario and have to be taken into account in future works of HD 45166. First, non-radial line forces might play an important role in shaping the 2D wind structure (Gayley & Owocki 2000). Secondly, if the star is rapidly rotating, the effective temperature will vary as a function of latitude (von Zeipel 1924), and the 2D wind structure will likely be affected.

8. Conclusions

In the following, we present the main conclusions of this paper.

1. We used the radiative transfer code CMFGEN to quantitatively analyze the wind of the qWR star HD 45166, and to constrain its fundamental parameters. Comparing the model spectrum with high-resolution optical observations, it was possible to determine the effective temperature, radius, luminosity, mass-loss rate, wind terminal velocity, and surface abundances. The temperature of the hot star is $T_{eff} = 50\,000 \pm 2000$ K, the radius is $R_{phot} = 1.00\,R_\odot$, and the luminosity is $\log(L/L_\odot) = 3.75 \pm 0.08$.

2. The wind parameters are quite anomalous. The mass loss rate determined is $\dot{M} = 2.2 \times 10^{-7}\,M_\odot\,yr^{-1}$, which is about 4 times higher than the value proposed by van Blerkom (1978). Analyzing the optical lines, we determined the terminal velocity of the wind to be $v_\infty = 425$ km s^{-1}, and not 1200 km s^{-1} as measured by Willis et al. (1989), since the optical spectrum shows no evidence of such a high-velocity wind. While for O-type and WR stars $v_\infty/v_{esc} > 1.5$, in the case of HD 45166 it is only 0.32. In addition, the efficiency of momentum transfer from the radiation field to the wind is $\eta = 0.74$, which is at least a factor of 4 lower than what is found for WR stars.

3. The star is helium-rich, with $N_H/N_{He} = 2.0$, obtained by simultaneously fitting the He II lines which are unblended, such as He II λ 4686, and those blended with hydrogen Balmer lines, such as He II + Hα λ 6560. The He content is consistent with the analysis of the He II Pickering lines, which shows that a significant abundance of hydrogen exists in the wind. The helium content of HD 45166 is 4 times higher than the abundance determined by van Blerkom (1978). The CNO abundances are quite peculiar, and very different from those of the Sun, of central stars of planetary nebulae, as well as of WN stars.

4. The wind of the qWR star is not spherically symmetric. Analyzing the observed line profile in comparison to model spectra computed in 2D geometry, we were able to infer the presence of an oblate wind, with a minimum density contrast of 8:1 from equator to pole. Taking into account our assumptions, higher density contrasts, for instance 16:1, cannot be discarded since they yield similar line profiles.

5. We also analyzed whether the wind terminal velocity changes as a function of latitude, but there is no clear evidence that this is the case. If we include a fast polar wind ($v_\infty = 1300$ km s^{-1}) and a slower equatorial wind ($v_\infty = 300$ km s^{-1}), the observed line profiles can be fitted with a lower density contrast from equator to pole of 4:1. Therefore, such a possibility might be a promising way to reconcile the values of v_∞ obtained from optical and UV analyses.

6. We applied the temporal variance spectrum (TVS) technique to the strongest emission lines of HD 45166. The TVS profiles of the lines are quite complex. The ratio sigma/intensity varies from 1.5% for He II lines up to 2.5% for those of He I. Both He I and He II lines also present a central dip in their TVS, in spite of this signature not being present in the intensity spectrum of He II.

7. The TVS of some emission lines, especially C IV, shows that variable absorption or scattering occurs near the equator; as a consequence, the red wings are more variable than the blue wings of the same line. The cause of this variability could be blobs of gas moving out in the wind compression zone or debris from variable mass transfer from the secondary star.

8. Differential gravitational redshift is seen in the velocities of high-ionization lines when compared to the velocities of low-ionization lines.

9. The latitudinal changes in the density and velocity might be explained by the formation of a wind compression zone (Ignace et al. 1996), which would imply that the qWR star has a relatively high rotational velocity.

References

Abbott, D. C., & Conti, P. S. 1987, ARA&A, 25, 113
Anger, C. J. 1933, Harvard College Observatory Bulletin, 891, 8
Bagnulo, S., Jehin, E., Ledoux, C., et al. 2003, The Messenger, 114, 10
Bjorkman, J. E., & Cassinelli, J. P. 1993, ApJ, 409, 429
Busche, J. R., & Hillier, D. J. 2005, AJ, 129, 454
Conti, P. S., Leep, M. E., & Perry, D. N. 1983, ApJ, 268, 228
Cox, A. N. 2000, Allen's astrophysical quantities (New York: AIP Press; Springer)
Crowther, P. A. 2007, ARA&A, 45, 177
Fullerton, A. W., Gies, D. R., & Bolton, C. T. 1996, ApJS, 103, 475
Gayley, K. G., & Owocki, S. P. 2000, ApJ, 537, 461
Georgiev, L. N., Hillier, D. J., & Zsargó, J. 2006, A&A, 458, 597
Grevesse, N., Asplund, M., & Sauval, A. J. 2007, Space Sci. Rev., 130, 105
Groh, J. H., Hillier, D. J., & Damineli, A. 2006, ApJ, 638, L33
Hillier, D. J. 1987, ApJS, 63, 947
Hillier, D. J. 1989, ApJ, 347, 392
Hillier, D. J., & Miller, D. L. 1998, ApJ, 496, 407
Ignace, R., Cassinelli, J. P., & Bjorkman, J. E. 1996, ApJ, 459, 671
Kaufer, A., Stahl, O., Tubbesing, S., et al. 1999, The Messenger, 95, 8
Lamers, H. J. G. L. M., & Cassinelli, J. P. 1999, Introduction to Stellar Winds (Cambridge, UK: Cambridge University Press)
Lamers, H. J. G. L. M., Snow, T. P., & Lindholm, D. M. 1995, ApJ, 455, 269
Marco, A., Negueruela, I., & Motch, C. 2007, in Active OB-Stars: Laboratories for Stellare and Circumstellar Physics, ed. A. T. Okazaki, S. P. Owocki, & S. Stefl, ASP Conf. Ser., 361, 388
Martins, F., & Plez, B. 2006, A&A, 457, 637
Oliveira, A. S., & Steiner, J. E. 2004, MNRAS, 351, 685
Osterbrock, D. E. 1989, Astrophysics of gaseous nebulae and active galactic nuclei (Mill Valley, Univ. Science Books)
Peimbert, M. 1990, Reports of Progress in Physics, 53, 1559
Pickles, A. J. 1998, PASP, 110, 863
Prinja, R. K., & Howarth, I. D. 1986, ApJS, 61, 357
Stahl, O., Kaufer, A., & Tubbesing, S. 1999, in Optical and Infrared Spectroscopy of Circumstellar Matter, ed. E. Guenther, B. Stecklum, & S. Klose, ASP Conf. Ser., 188, 331
Steiner, J. E., & Oliveira, A. S. 2005, A&A, 444, 895
van Blerkom, D. 1978, ApJ, 225, 175
von Zeipel, H. 1924, MNRAS, 84, 665
Willis, A. J., & Stickland, D. J. 1983, MNRAS, 203, 619
Willis, A. J., & Burnley, A. W. 2006, in Astrophysics in the Far Ultraviolet: Five Years of Discovery with FUSE, ed. G. Sonneborn, H. W. Moos, & B.-G. Andersson, ASP Conf. Ser., 348, 139
Willis, A. J., Howarth, I. D., Stickland, D. J., & Heap, S. R. 1989, ApJ, 347, 413
Zsargó, J., Hillier, D. J., & Georgiev, L. N. 2006, A&A, 447, 1093

Appendix A: The H/He abundance and the He II Pickering decrement

The hydrogen abundance determined by van Blerkom (1978) is $N_H/N_{He} \sim 5.3$ (by number), which is about 4 times higher than the value derived through the detailed radiative transfer modeling using CMFGEN ($N_H/N_{He} = 2.0$ by number, see Sect. 4.4). This difference is significant, and we will analyze the He II Pickering decrement to verify this discrepancy.

Although the hot star of HD 45166 is He-rich (65% in mass, at least in the wind), the presence of hydrogen is an important aspect to be carefully considered in the analysis. As mentioned by Willis & Stickland (1983), judging from the He II Pickering decrement, hydrogen is definitely present. To check this, we compared our observations with the expected theoretical values. For practical reasons we normalized the predicted and the observed values to 1 for He II λ 5411. Figure A.1 shows the comparison between the two series, and we clearly see the typical oscillation pattern that appears when hydrogen is present. It is also possible to infer that the intensities of the lines that coincide with hydrogen Balmer lines are about twice as strong as the expected ones if there was no Balmer emission. One way of analyzing the presence of hydrogen in a helium-rich wind spectrum, following Oliveira & Steiner (2004), is by defining the Pickering parameter, p:

$$p = \frac{I(4859 + 4861)}{[I(4541).I(5411)]^{0.5}} .$$ (A.1)

Using the predicted theoretical intensities that one expects for a pure He II spectrum, calculated for a low-density gas, $p = 0.97 \pm 0.01$ (Osterbrock 1989). Any value of p larger than 1 would mean hydrogen is present in the wind. In the case of HD 45166, the measured value is $p \simeq 2.95$. If both H and He lines were optically thin, it would be easy to determine the relative abundance between the two species. In this case, given the specific emissivity of the respective transitions (Osterbrock 1989),

$$\frac{N(H+)}{N(He^{++})} = p - 1.$$ (A.2)

For HD 45166, one gets $N(H^+)/N(He^{++}) \simeq 1.95$. The largest uncertainty in this value is the hypothesis that all of the involved lines are optically thin. This may be a good approximation in the wings of the lines but not in their cores. For an optically thick case we have (Conti et al. 1983):

$$\frac{N(H+)}{N(He^{++})} = p^{1.5} - 1.$$ (A.3)

and thus we obtain $N(H^+)/N(He^{++}) \simeq 4.06$.
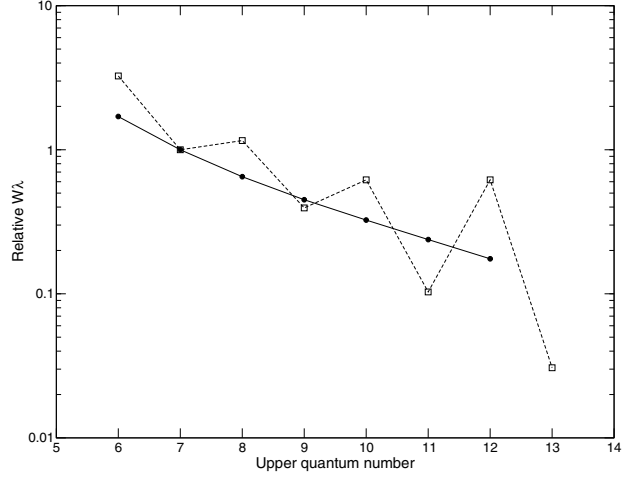
Fig. A.1. Intensity of the He II lines of the Pickering series as a function of the upper quantum number, normalized such that I(He II λ 5411) = 1. The open squares represent the observed values of HD 45166, the filled circles correspond to the theoretical prediction for an optically-thin gas, using tabulated values from Oliveira & Steiner (2004).

Appendix B: The CNO emission line table
for HD 45166

Table B.1. Equivalent width of the CNO emission lines in HD 45166 obtained from the observations. References: Willis & Stickland (1983) for ultraviolet lines (1200–3300 Å), and this work for optical lines (3700–9000 Å). Key: y = *line* is present; y? = doubtful identification due to low S/N; ? = doubtful identification due to presence of a telluric line; bl = blended with other lines; n=line is definitely not present.

Term	$J-J$	O λ (Å)	O W_λ (Å)	N λ (Å)	N W_λ (Å)	C λ (Å)	C W_λ (Å)
		O III					
IP(eV)		54.94					
Singlets							
1P^0–1S	1–0	1247	?				
3s 1P^0–3p 1P	1–1	5592	0.75				
3p 1D–3d 1F^0	2–3	3962	0.29				
4p 1S–5s1P^0	0–1	5268	0.13				
4p 1D–5s 1P^0		4569	0.05				
3s 1P^0–3p 1D		2984	0.88?				
Triplets							
3P^0–3P		1175	1.86 ?				
3s 3P^0–3p 3D	2–3	3760	1.4				
	1–2	3755	0.99				
	0–1	3757	1.1				
	2–2	3791	…				
	1–1	3774	…				
3p 3P–3d 3D^0	2–3	3715	0.99				
	1–2	3707	0.35				
	1–1	3703	…				
3s 3P–3p 3D^0	2–3	4081	0.12				
		4074	…				
4d 3P^0–3s 3D	1–2	7455	0.08				
		7475	…				
		7482	…				
		7492	…				
		O IV		N III			
IP(eV)		77.41		47.45			
2p2 2P–2p3 2Do	3/2–5/2	1344	…	1752	…		
	1/2–3/2	1339	1.82	1748	…		
	3/2–3/2	1343	0.92	1751	…		
3s 2S–3p 2P^0	1/2–3/2	3063	…	4097	1.66		
	1/2–1/2	3072	…	4103	0.84		
3s 2P^0–3p 2D	3/2–5/2	3349	…	4200	0.77		
	1/2–3/2	3348	…	4196	0.16		
	3/2–3/2	3378	…	4216	…		
3p 2P–3d 2P^0	3/2–3/2	2133	…	2984	0.88		
	1/2–3/2	2127	…	2979	…		
	3/2–1/2	2126	…	2977	…		
	1/2–1/2	2120	…	2973	…		
3p 2P^0–3d 2D	3/2–5/2	3412	…	4641	1.37		
	1/2–3/2	3404	…	4634	0.75		
	3/2–3/2	3414	…	4642	?		
4d 2D–5f 2F^0	5/2–7/2	3563	…	4004	0.07		
	3/2–5/2	3560	…	3999	…		
4f 2F^0–5g 2G				4379	0.56		
3d 2P^0–6d 2D				8494	y		
5f 2F^0–6g 2G				8019	0.54		
3s 4P^0–3p 4D	5/2–7/2	3386	…	4515	0.19:		
	1/2–3/2	3381	…	4511	0.21		
3p 4D–3d 4F^0	7/2–9/2	3737	…	4867	0.20		
	5/2–7/2	3729	…	4861	…		
	3/2–5/2	3725	…	4859	…		
		O v		N IV		C III	
IP(eV)		113.90		77.47		47.89	
Singlets							
2p 1P^0–2p2 1D	1–2	1371	2.71	1719	4.97	2297	1.88

Table B.1. continued.

Term	$J-J$	O λ (Å)	O W_λ (Å)	N λ (Å)	N W_λ (Å)	C λ (Å)	C W_λ (Å)
2p 1P⁰–2p2 1S	1–0	774	...	955	...	1247	y
3s 1S–3s 1P⁰	0–1			1188	0.19	1591	...
3s 1S–3p 1P⁰	0–1	5114	y?	6381	0.21:	8500	y
3p 1P⁰–3d 1D	1–2	3145	...	4058	1.11	5695	0.096
3d 1D–3s 1P⁰				2279	...	2982	y?
3d 1D–3d 1F⁰	2–3			1310	0.26	1541	...
3d 1D–5f 1F⁰	2–3	509	...	1297	y?	1382	...
4p 1P⁰–5d 1D	1–	1419	0.30				
4f 1F⁰–5g 1G	3–4	1708	...	3078	...	4187	0.127
Intercombination							
2s2 1S–2p 3P⁰	0–	1218	...	1486	0.11	1909	n
Triplets							
2p 3P⁰–2p2 3P	1–0	759	...	923	...	1175	1.86
		759	...			1172	...
3s 3S–3p 3P⁰	1–2	2781	...	3479	...	4647	2.38
	1–1	2787	...	3482	...	4650	1.46
	1–0	2790	...	3484	...	4651	0.42:
3s 3P⁰–3p 3P	2–2	2731	...	3463	y	4666	y
		2744	...	3461	y	4673	?
		2729	...	3475	y	4663	?
3s 3P⁰–3p 3D	2–3	4124	...	5204	y	6744	0.17
		4120	...	5200	y	6731	0.077:
		4125	...	5205	y?	6727	...
3p 3P⁰–3p 3D		1055	...	1272	0.92	1578	...
		1058	...				
		1059	...				
		1060	...				
		1061	...				
3p 3P⁰–3d 3D	2–3	5598	n	7123	3.31	9715	...
	1–2	5580	...	7109	1.91:	9705	...
	0–1	5573	...	7103	0.92	9701	...
	2–2	5604	...	7127	0.70:	9718	...
	1–1	5583	...	7111	y	9706	...
	2–1	5607	...	7129	...	9719	...
3d 3D–3d 3F⁰				1326	0.14		
3d 3D–5f 3F⁰						1296	...
4s 3S–4p 3P⁰	1–2	7437	n	6220	y	7796	n
	1–1	7443	n	6215	y	7780	n
	1–0	7458	...	6212	y?	7772	...
4p 3P⁰–5d 3D	2–	1418	0.61	2036	...	3610	...
4d 3D–5f 3F⁰		1507	0.37	2318	...	3889	y?
5d 3D–6f 3F⁰		2757	...			7487	0.134
4f 3F⁰–5g 3G	4–5	1644	...	2648	...	4068	y
				2647	...	4070	y
				2646	...		
5f 3F⁰–6g 3G		2707	...	4707	y	7487	y
5g 3G–6h 3H⁰		2942	...	4606	0.077	8196	y
6h 3H⁰–7i 3I		4930	y	7703	y	13696	...

				N v		C iv	
IP(eV)				97.89		64.49	
Doublets							
2s 2S– 2p 2P⁰	1/2–3/2			1239	9.0	1548	1.34
	1/2–1/2			1243	...	1551	0.55
3s 2S–3p 2P⁰	1/2–3/2			4604	abs	5801	16.68
	1/2–1/2			4620	abs	5812	9.96
4s 2S–4p 2P⁰	1/2–3/2			11331	...	14335	...
	1/2–1/2			11374	...	14362	...
5s 2S–5p 2P⁰	1/2–3/2			22572	...	28617	...

Table B.1. continued.

Term	$J - J$	O λ (Å)	O W_λ (Å)	N λ (Å)	N W_λ (Å)	C λ (Å)	C W_λ (Å)
	1/2–1/2			22654	...	28675	...
Multiplets							
(4–5)				1620	0.21	2530	0.26
				1622	0.15		
				1655	...		
(5–6)				2981	...	4658	0.42:
(5–7)				1860	...	2907	...
(6–7)				4945	0.103	7726	1.55
(6–8)				2998	...	4685	bl
(7–8)				7618	...	1908	...
(7–9)				4520	...	7063	y
(8–9)				10980	...	17371	...
(7–10)				3502	...	5471	y
(8–10)				6478	...	10124	...
(9–10)				15536	...	24278	...
(8–11)				4943:	...	7737	y
(9–11)				8927	...	13954	...
(10–11)				21000	...	32808	...
(8–12)				4191	...	6560	bl
(9–12)				6747	...	10543	...
(10–12)				11928	...	18635	...
(11–12)				27593	...	43138	...
(9–13)				5670	...	8858	...
(10–13)				8918	...	13946	...